Electronic Supplementary Material (ESI) for Journal of Materials Chemistry A.
This journal is © The Royal Society of Chemistry 2019

# Electronic Supplementary Information

# Immobilization of Co, Mn, Ni and Fe oxide co-catalysts on $TiO_2$ for photocatalytic water splitting reactions

Jasmin S. Schubert,[a] Janko Popovic,[a] Greta M. Haselmann,[a] Sreejith P. Nandan,[a] Jia Wang ,[a]
Ariane Giesriegl,[a] Alexey S. Cherevan*[a] and Dominik Eder*[a]

[a] Institute of Materials Chemistry, Technical University of Vienna, Getreidemarkt 9, 1060,
Vienna, Austria

## A list of supplementary Figures:

## A list of supplementary Tables:

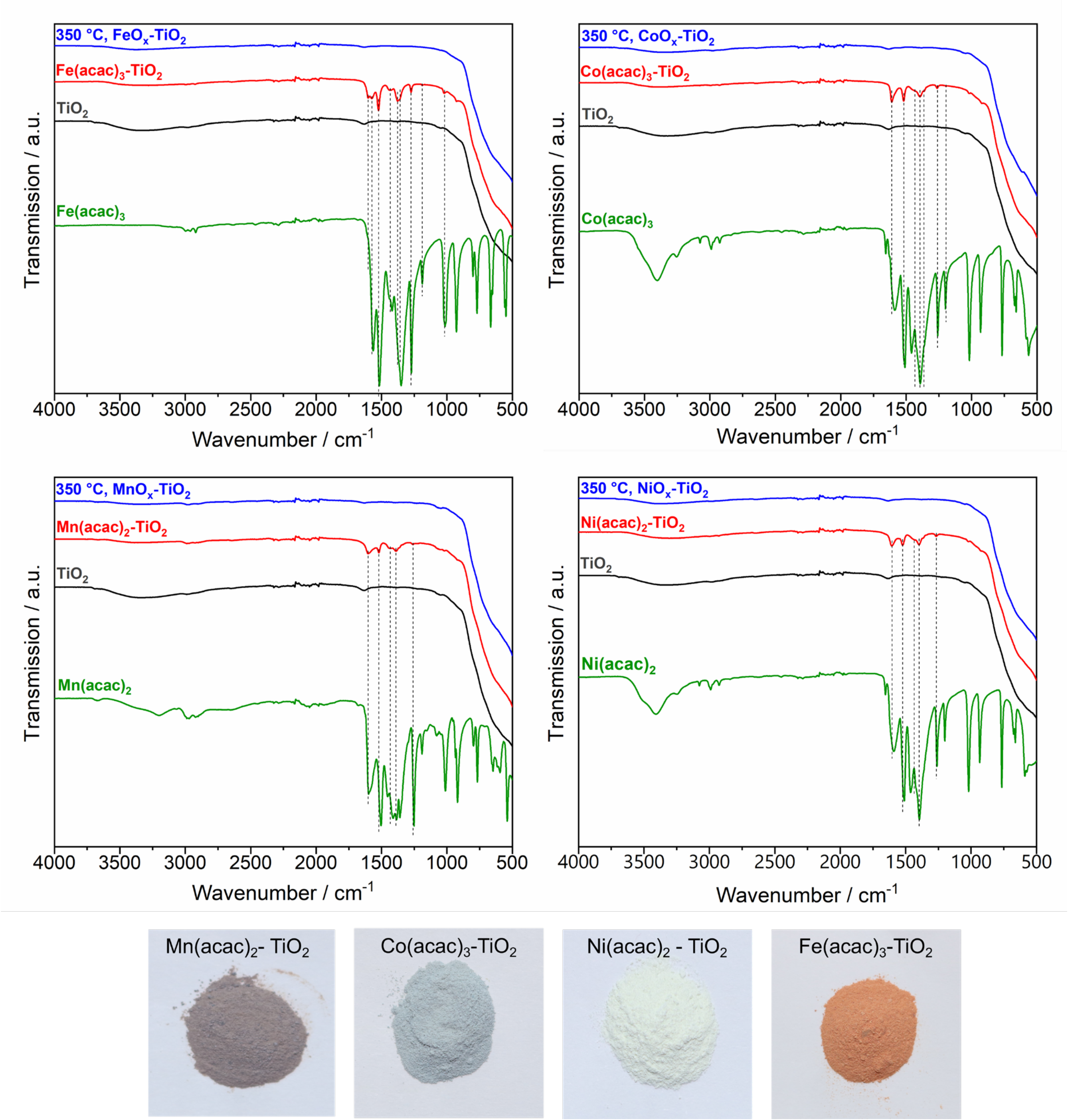

**Figure S1.** *On the top:* ATR-FTIR spectra of the obtained composites along with the original salts, reference $TiO_2$, photocatalyst powder before calcination (M(acac)$_x$-$TiO_2$, with M corresponding to Co, Mn, Fe and Ni) and after calcination ($MO_x$-$TiO_2$). The reference M(acac)$_x$ salts show the characteristic C=O band (1572.5 cm$^{-1}$ for Fe(acac)$_3$, 1589.2 cm$^{-1}$ for Co(acac)$_3$, 1598.8 cm$^{-1}$ for Mn(acac)$_2$ and 1594.0 cm$^{-1}$ for Ni(acac)$_2$) and the fingerprint region from 1700 cm$^{-1}$ to 500 cm$^{-1}$ of the organic ligand. The presence of the acetylacetonate is also visible in the M(acac)$_x$-$TiO_2$ composites between 1700 cm$^{-1}$ and 1120 cm$^{-1}$. The band at 3412.7 cm$^{-1}$ for Ni(acac)$_2$ and 3409.5 cm$^{-1}$ for Co(acaca)$_3$ correspond to the presence of crystalline water. After calcination at 350 °C, the absence of acetylacetonate signals can be assigned to its complete oxidation. *On the bottom:* photographs of the $TiO_2$ composites after impregnation with the different metal precursors before calcination.

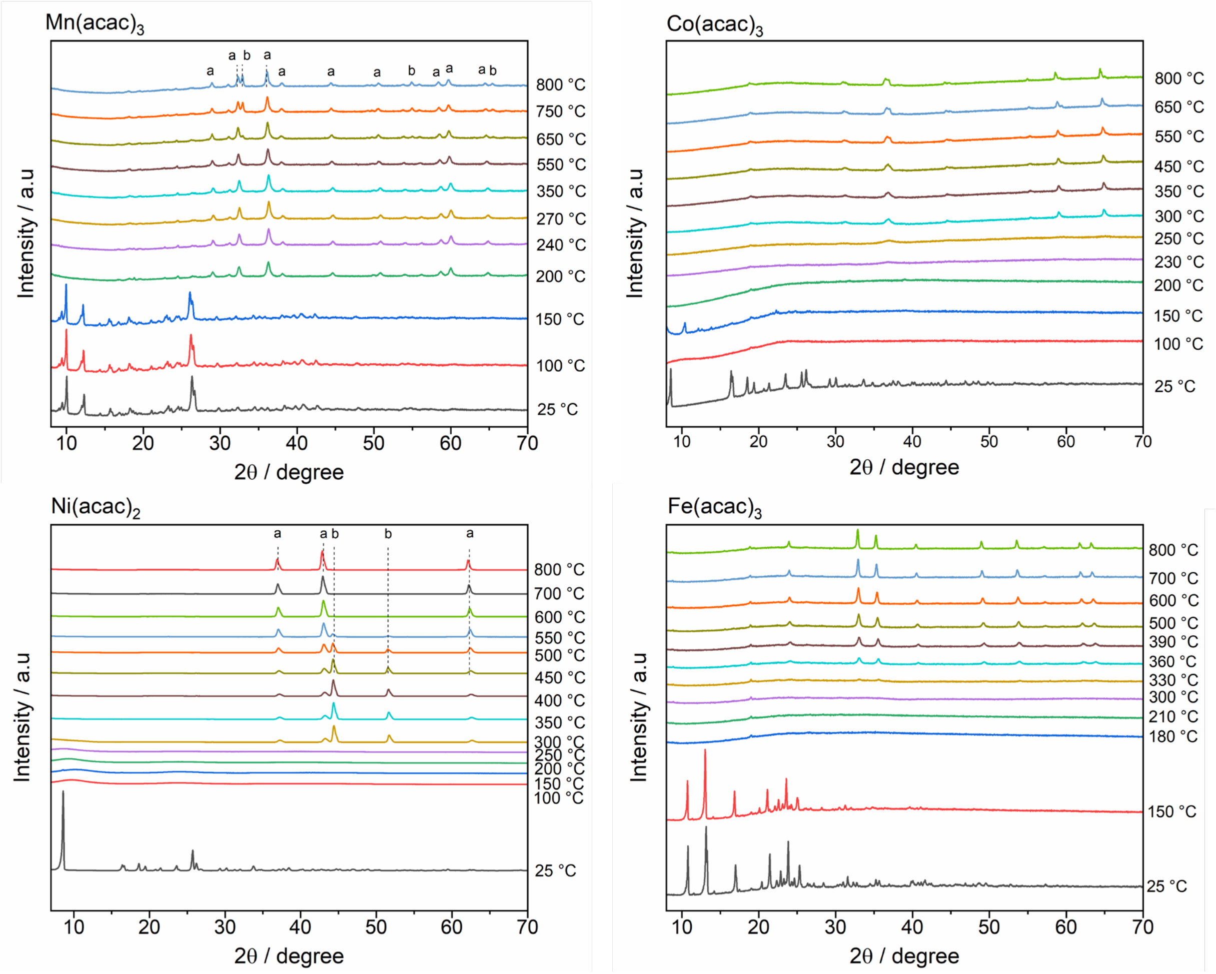

**Figure S2.** Complete data sets of the in situ XRD experiments performed for pure acetylacetonate precursors (Mn(acac)$_2$, Co(acac)$_3$, Ni(acac)$_2$ and Fe(acac)$_3$). The data was recorded at air with a 5°C/min heating rate and temperature range from 25 °C to 800 °C. Legend: **a**: $Mn_3O_4$ , NiO , **b**: $Mn_2O_3$ , Ni.

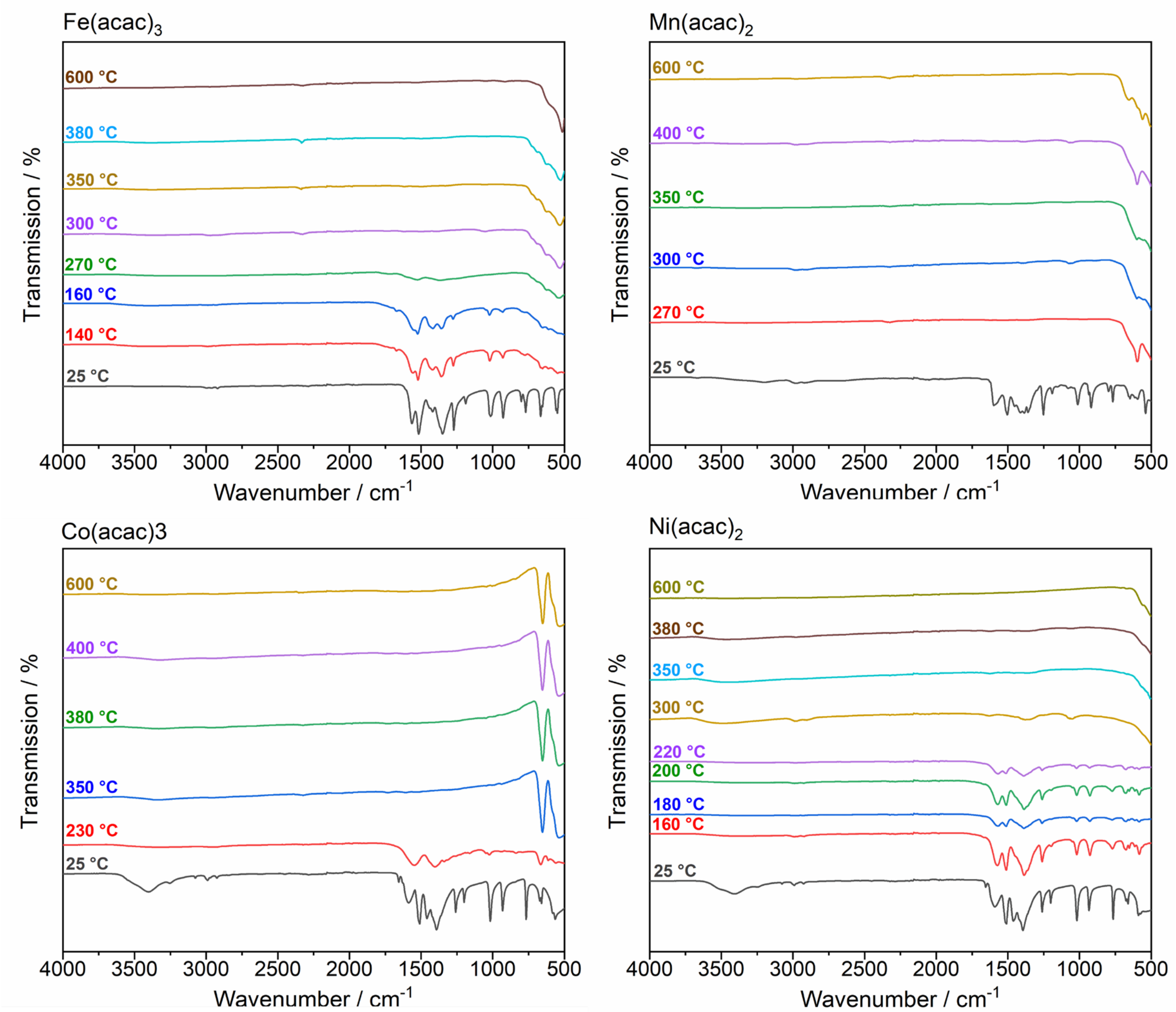

**Figure S3.** *Quasi in situ* ATR-FTIR spectra showing the thermal decomposition of the original salt precursors precursors ( Mn(acac)$_2$, Co(acac)$_3$, Ni(acac)$_2$ and Fe(acac)$_3$) calcined at a temperature range from 25 °C to 600 °C.

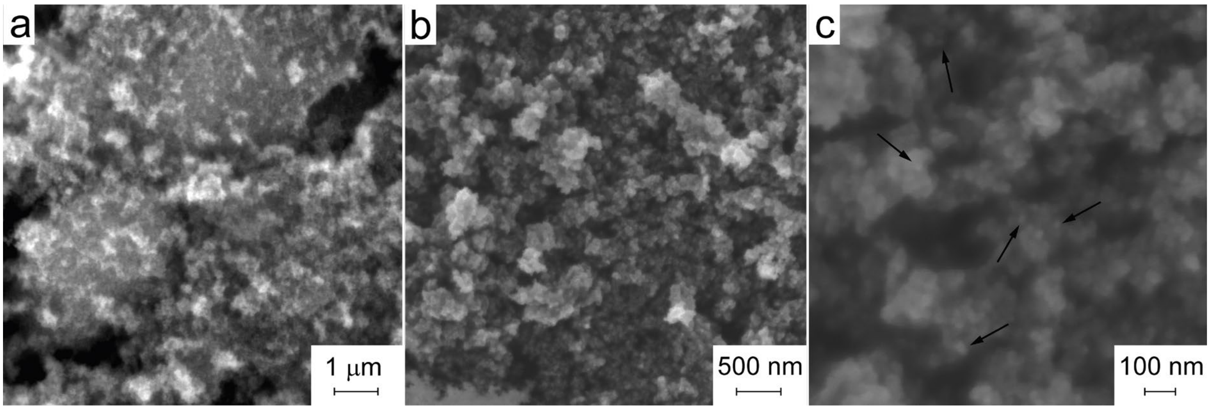

**Figure S4.** SEM of the FeO$_x$-TiO$_2$ sample representative for the rest of the composites. The images reveal the presence of nanoparticle aggregates corresponding to typical TiO$_2$ nanopowder. Image (c) shows individual TiO$_2$ nanoparticles with expected dimensions (20-50 nm). No foreign particles has been generated upon the composite formation.

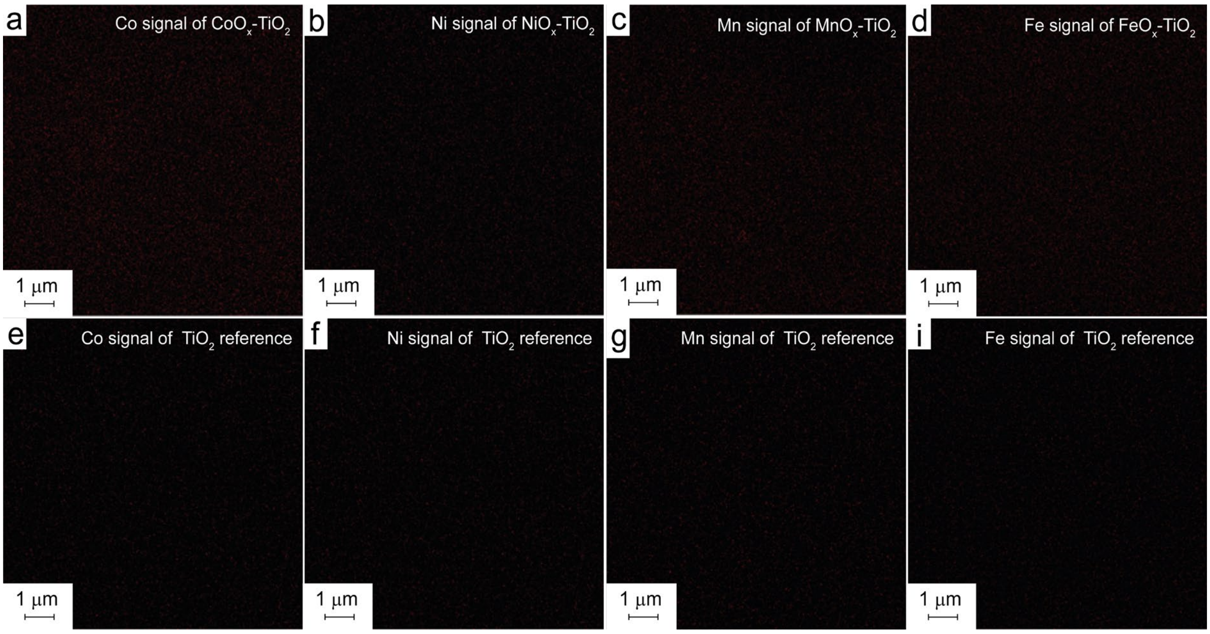

**Figure S5.** EDX mapping of the CoO$_x$-TiO$_2$ (a), NiO$_x$-TiO$_2$ (b), MnO$_x$-TiO$_2$ (c), and FeO$_x$-TiO$_2$ (d) nanocomposites along with the Co (e), Ni (f), Mn (g) and Fe (i) EDX signals acquired for pure reference TiO$_2$ powder. The images on the bottom are not related to the actual presence of these elements in TiO$_2$, but rather originate from the data acquisition process and "non-zero" background signal of the EDX scans.

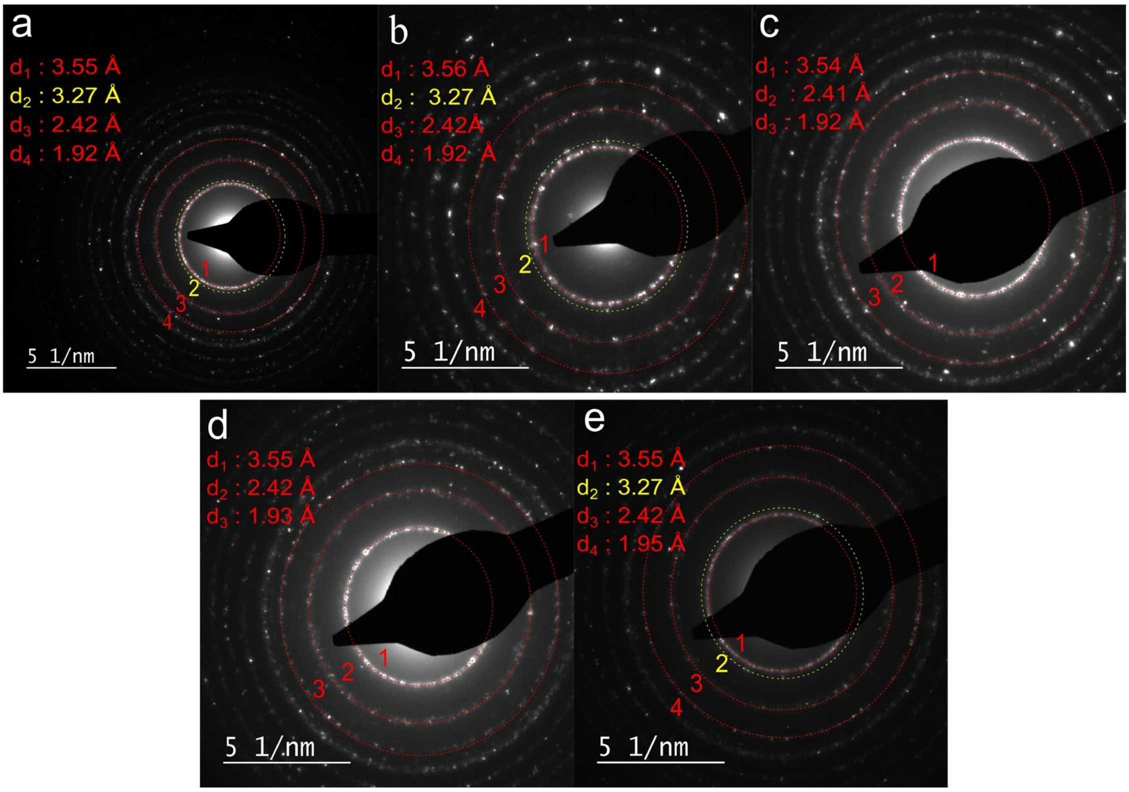

**Figure S6.** Electron diffraction (ED) pattern of the MO$_x$ -TiO$_2$ composite. (a) Pure TiO$_2$, (b) NiO$_x$ -TiO$_2$, (c) MnO$_x$ -TiO$_2$, (d) FeO$_x$ -TiO$_2$ and (e) CoO$_x$ -TiO$_2$ revealing that all samples show the corresponding d values of the TiO$_2$ anatase phase (red) and rutile (yellow). The anatase phase is much more intense in all samples indicating a much higher concentration in the sample, while the rutile phase is present in a much lower amount, as can be seen by the much less intense signal.

## Discussion of Raman data

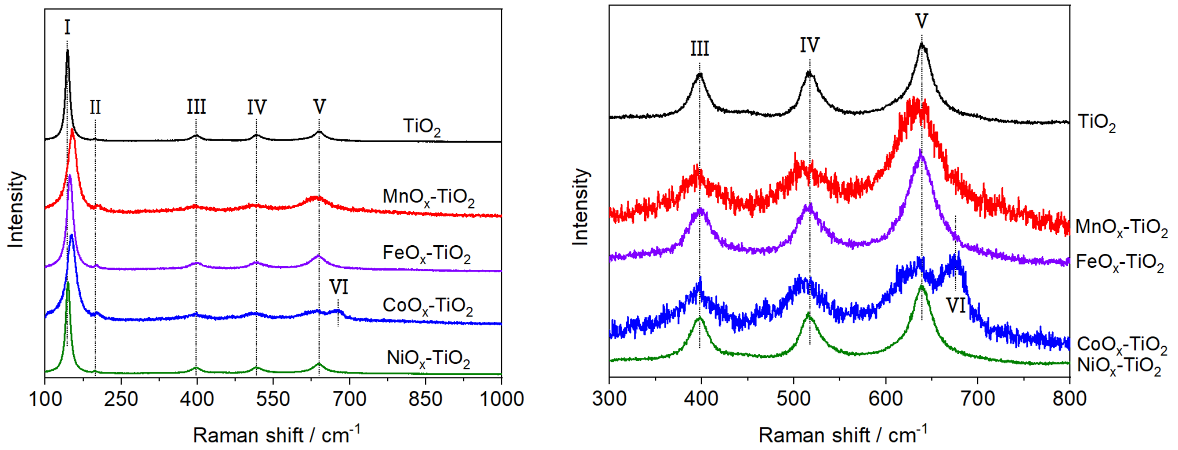

**Figure S7.** Raman spectra of the $MnO_x$-$TiO_2$, $FeO_x$-$TiO_2$, $CoO_x$-$TiO_2$ and $NiO_x$-$TiO_2$ composites along with the $TiO_2$ reference. (a) Overview spectra. (b) Magnified regions.

In $TiO_2$ reference spectrum, peaks present at around 144, 198, 397, 517 and 640 $cm^{-1}$ can be assigned to the $E_g$, $E_g$, $B_1$, $A_{1g}+B_{1g}$ and $E_g$ modes of anatase phase, respectively (**Figure S7**), while the peak present at 448 $cm^{-1}$ can be attributed to the $E_g$ mode of rutile phase, in line with $TiO_2$ composition. **Table S1** presents a summary of the peak positions and peak full-width at half-maxima (FWHM) of the strongest anatase $E_g$ band of the $TiO_2$ reference as well as the rest of the $MO_x$-$TiO_2$ composites:

**Table S1.** Peak analysis of the as-prepared $MO_x$-$TiO_2$ composites along with $TiO_2$.

| | I ($E_g$) | II ($E_g$) | III ($B_{1g}$) | IV ($A_{1g}+B_{1g}$) | V ($E_g$) | VI | FWHM of peak I ($E_g$) |
|---|---|---|---|---|---|---|---|
| **$TiO_2$** | 144 | 198 | 397 | 517 | 640 | | 9.5 |
| **$MnO_x$-$TiO_2$** | 153 | 203 | 397 | 512 | 636 | | 22.3 |
| **$FeO_x$-$TiO_2$** | 150 | 202 | 398 | 515 | 637 | | 17.3 |
| **$CoO_x$-$TiO_2$** | 152 | 204 | 396 | 512 | 631 | 673 | 22.3 |
| **$NiO_x$-$TiO_2$** | 144 | 198 | 398 | 517 | 639 | | 10.5 |

It can be seen from **Table S1** that, compared with $TiO_2$, all $MO_x$-$TiO_2$ samples demonstrate substantial peak shifts (blue-shifts for peak 'I' and 'II', red-shifts for peak 'IV' and peak 'V'), except for $NiO_x$-$TiO_2$ sample. As an example, the shift of the most intense $E_g$ band (I) can be considered.

It is known that the peak shift in Raman can be caused by different reasons, including the crystallite size,[1] crystal strain,[2] non-stoichiometry/doping,[3] surface adsorbed species,[1] etc. It is also known that the FWHM of the anatase $E_g$ mode (~ 146 $cm^{-1}$) reflects the stoichiometric ratio of O/Ti.[4] In the oxidation annealing experiment of $TiO_{2-x}$ performed by Parker and Siegel,[4] the authors have discovered that the FWHM above 13 $cm^{-1}$ indicates that the oxide is oxygen deficient ($x > 0$); and the higher the FWHM value is, the higher does the oxygen deficiency (x) get. The substantially larger FWHM values of $MO_x$-$TiO_2$ (for Mn, Fe, Co) therefore suggest that the samples may have oxygen deficiency.

Overall, considering our composite systems, the data for $MnO_x$-$TiO_2$, $CoO_x$-$TiO_2$ and $FeO_x$-$TiO_2$ may suggest the presence of additional (apart from those observed in TEM) surface-adsorbed species on $TiO_2$, creation of O vacancies or bulk doping with M ions.

More specifically for each of the composites (see **Figure S7**):

***$MnO_x$-$TiO_2$:***

The observed broadening/shoulder of the peak IV at 512 cm$^{-1}$ and peak V at 640 cm$^{-1}$ can be assigned to newly formed $MnO_x$ species decorating $TiO_2$ surface. These bands may be caused by various $MnO_x$ phases incl. manganite, pyrolusite or todorokite.[5] However, given the similarity in the band position of different $MnO_x$ species,[5] especially in light of the amorphous nature of the $MnO_x$ clusters in our composites, it seems incorrect to make any assumption about the possible phase or even oxidation state of Mn species. Besides this, $MnO_x$ have low Raman activity and are known for their high sensitivity to the laser-induced heating, which can easily cause shifts and broadening of the Raman peaks and thus unreliable interpretation of the Raman data.

***$FeO_x$-$TiO_2$:***

Compared with the Raman spectra of $TiO_2$, no additional band corresponding to $FeO_x$ have been detected. On the other hand, the observed peak broadenings of $TiO_2$ bands is also unlikely caused by the potential Raman bands of $FeO_x$ due to the position mismatch. No further conclusions can be made.

***$CoO_x$-$TiO_2$:***

Additional shoulder and peak arising at 470 cm$^{-1}$ and 673 cm$^{-1}$, respectively, can be assigned to the $Co_3O_4$,[6] in line with our expectations. Compared with the standard position of the $A_{1g}$ band of crystalline $Co_3O_4$ expected at 680 cm$^{-1}$, the shifted vibrational band at 673 cm$^{-1}$ of our $CoO_x$-$TiO_2$ may indicate for the highly defective structure,[6] in line with the amorphous nature, surface distribution and mixed composition of our $CoO_x$ clusters. In addition, referring to XPS data, $Co^{2+}$ could be present as dopant in the $TiO_2$ lattice. Due to the larger ionic radius of $Co^{2+}$ (0.885Å), substitutional $Co^{2+}$ dopants would tend to distribute on the surface of $TiO_2$, which would further lead to the formation of surface oxygen vacancies and surface disorder reflected in the shift of the $TiO_2$ $E_g$ band in the Raman spectra.[7] Surface $Co^{2+}$ species could also take part in the observed OER.[7]

***$NiO_x$-$TiO_2$:***

Especially interesting result was observed for $NiO_x$-$TiO_2$ composites whose Raman spectra did not resemble the behaviour observed for the rest of the composites (i.e. peak shifts and broadening of main $TiO_2$ bands), but looked rather identical to the reference $TiO_2$ powder.

Typically, signal broadening, decreased intensity and the peak shifts of $TiO_2$ bands may be indicative of the presence of doping, oxygen vacancies and other structural defects and disorders as well as crystal strain and surface adsorbed species. As mentioned before, some of these effects can take place in our $MO_x$-$TiO_2$ composites, but, surprisingly, there is no indication of these for the $NiO_x$-$TiO_2$ sample. Why does not this particular samples exhibit this kind of behaviours that could be expected for surface-immobilized amorphous $MO_x$ species?

According to our TEM results, $NiO_x$-$TiO_2$ sample features extremely small, but well defined NPs with the size of about 1 to 2 nm. Such homogeneity of the particle size and their fine distribution may indicate that the formed $NiO_x$ NPs are thermodynamically stable and have reached a certain optimal size during the precursor decomposition, followed by nucleation and growth of the $NiO_x$. If this process is energetically favourable, all Ni species would be consumed to form these NPs and one could expect neither Ni incorporation into the $TiO_2$ matrix (doping) nor presence of atomic Ni-based species over the $TiO_2$ surface, thus explaining no shifts or peak broadenings of the substrate $TiO_2$. Further investigation is required to understand this exceptional behaviour.

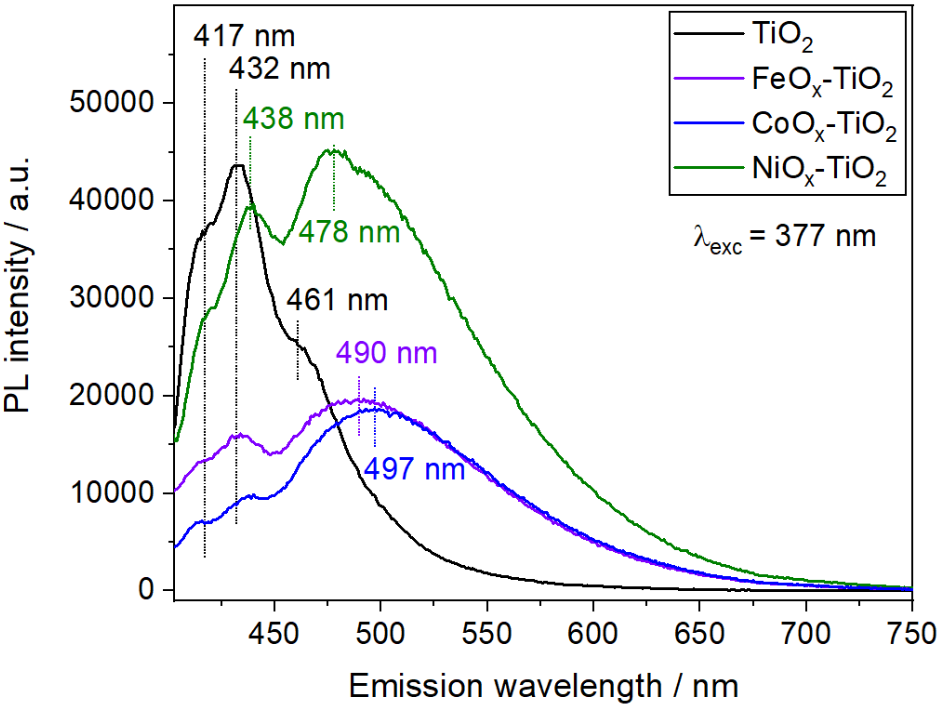

**Figure S8.** Steady-state photoluminescence (PL) spectra of the $FeO_x$-$TiO_2$, $CoO_x$-$TiO_2$ and $NiO_x$-$TiO_2$ composites along with the $TiO_2$ reference.

## Discussion about the crystallinity of the obtained $MO_x$ species

To elucidate a possible reason why the resulting composites feature amorphous $MO_x$ NPs, we have subjected the pure $Ni(acac)_2$ salt precursor to the same synthetic procedure than the composites (but without $TiO_2$ present) and analysed the dried product after solvent evaporation with XRD. The data in **Figure S9b** revealed that indeed the salt losses its crystalline structure after being recollected as a powder. This, in turn, can explain why the resulting oxides after calcination may be of amorphous nature. The amorphous nature was also confirmed by synthesised model composites - using $Ni(acac)_2$-$TiO_2$ - with an increased amount of $Ni(acac)_2$ up to 24.4 wt. %. The x-ray diffractograms of these model systems showed only the presence of $TiO_2$ (rutile and anatase, **Figure S9b** and **c**) for both thermal treated and untreated samples. Thus, with these model system investigations, it can be confirmed that the generated metal species in our composites are indeed amorphous.

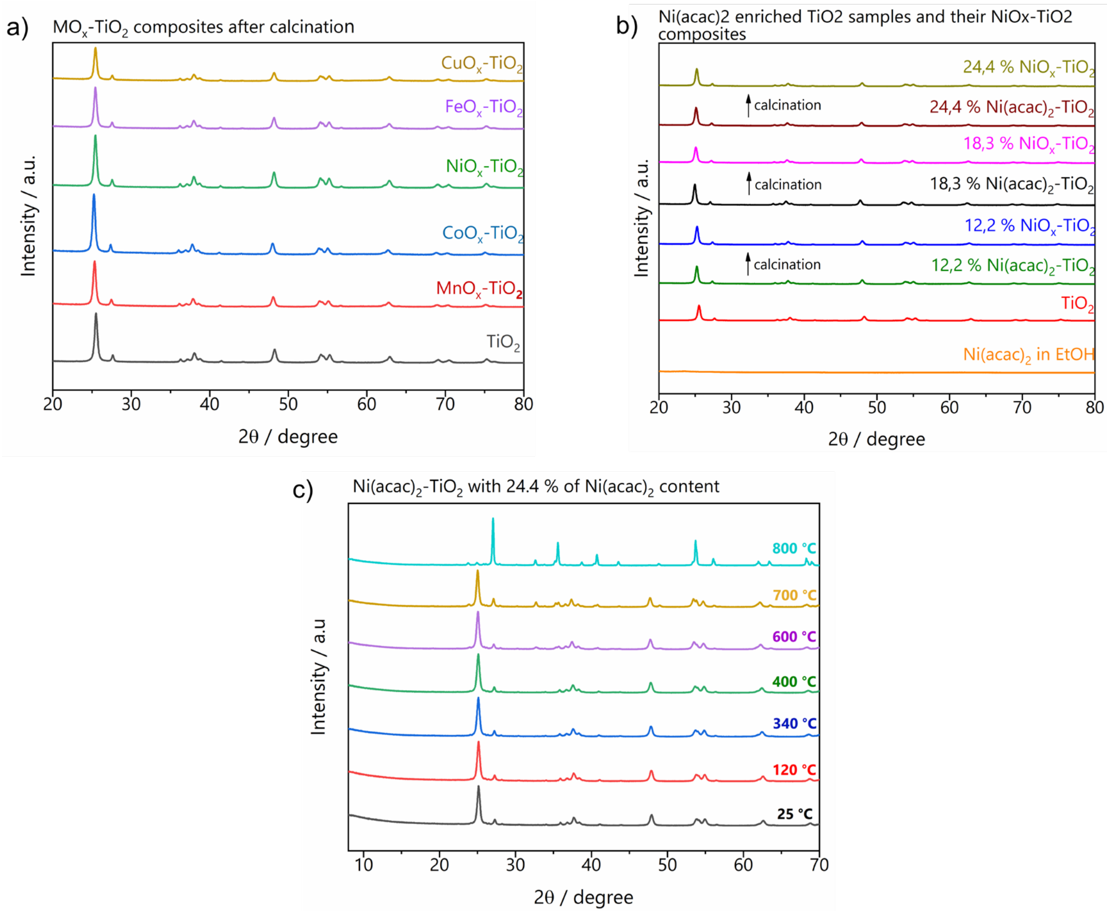

**Figure S9.** (a) XRD data of the $MO_x$-$TiO_2$ composites (prepared at 350 °C) and the $TiO_2$ reference to demonstrate the incapability of XRD to detect the newly deposited species. (b) Pure $TiO_2$ as reference material and the corresponding $Ni(acac)_2$-$TiO_2$ as well as $NiO_x$-$TiO_2$ composites after calcination demonstrating that even higher precursor loadings do not yield XRD signals that can be attributed to $NiO_x$ species. The diffractogram on the bottom corresponds to the $Ni(acac)_2$ salt after dissolution in ethanol showing that the originally crystalline salt loses its crystal structure after being recollected. (c) *In situ* XRD data of the $Ni(acac)_2$-$TiO_2$ composite with 24.4 wt. % $Ni(acac)_2$ content (heating rate 5°C/min at air) from 20 °C to 800 °C: only signals corresponding to $TiO_2$ (anatase and rutile) are visible in the spectra. Importantly, XRD profile starts changing (new peaks appear) above roughly 500 °C, which is exclusively related to gradual anatase-to-rutile conversion.

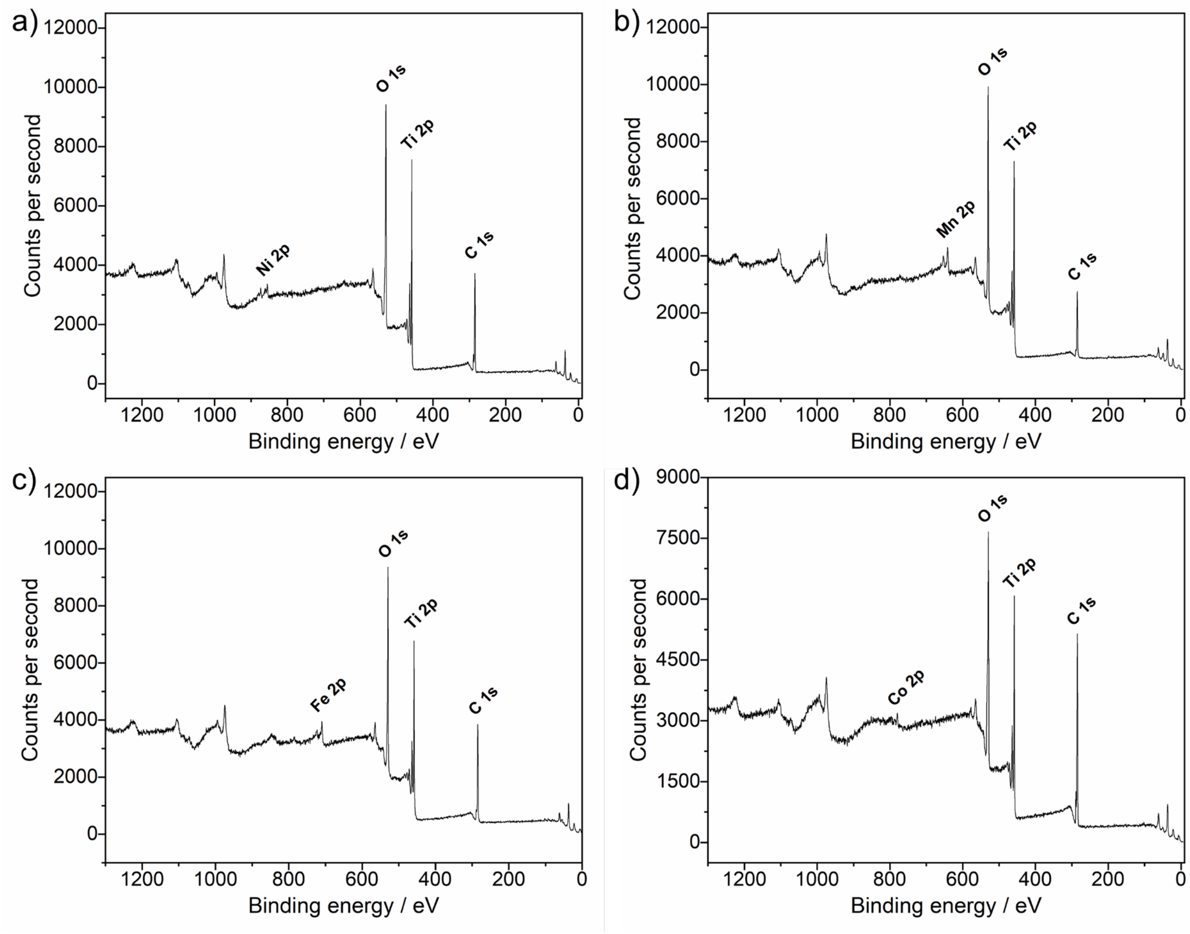

**Figure S10.** Survey XPS spectra of the (a) $NiO_x$ -$TiO_2$, (b) $MnO_x$ -$TiO_2$, (c) $FeO_x$ -$TiO_2$ and (d) $CoO_x$ -$TiO_2$ composites.

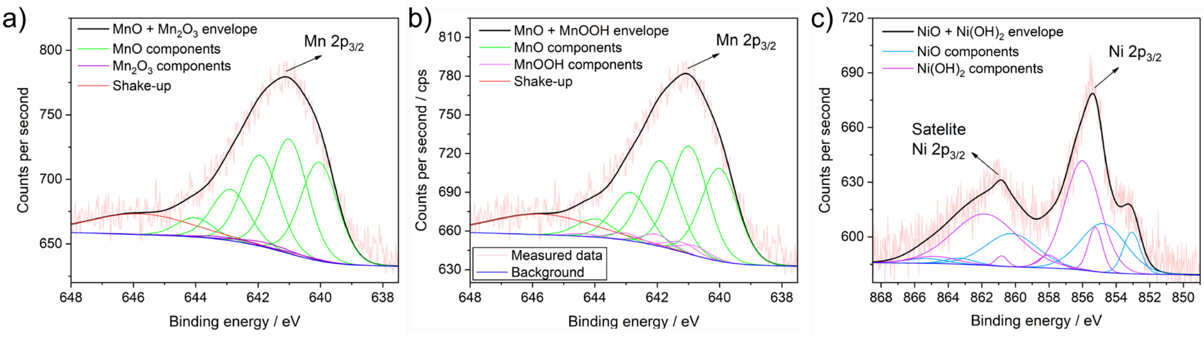

**Figure S11.** XPS spectra with the corresponding fits. a) and b) 2p Mn from the $MnO_x$-$TiO_2$ composite. c) Ni 2p spectra of $NiO_x$-$TiO_2$ composite.

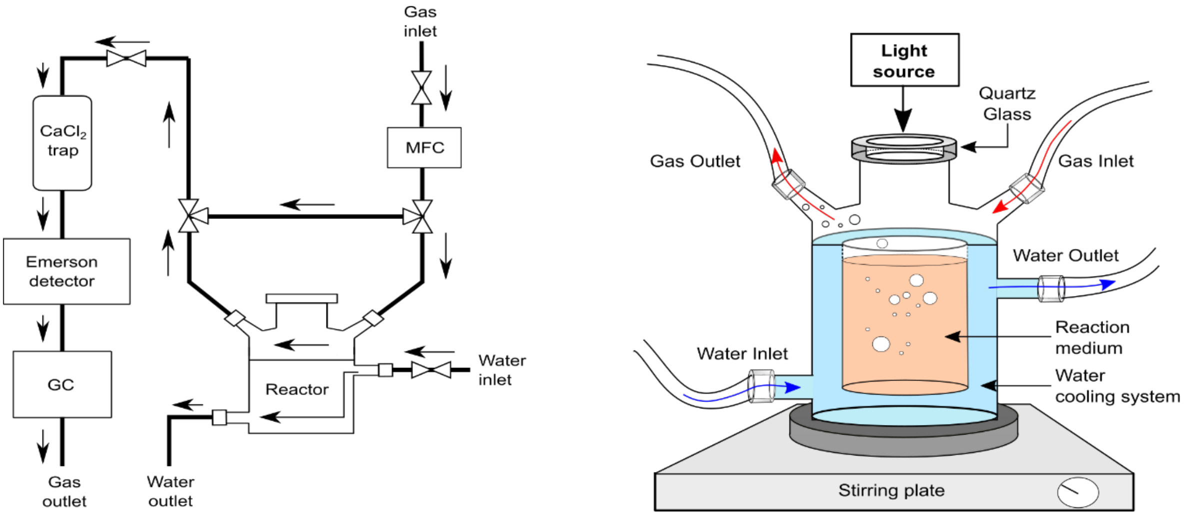

**Figure S12.** Experimental setup for the hydrogen evolution reaction (HER) experiments that were performed in flow-mode (see Methods). The oxygen evolution reactions (OER) experiments were performed in the same reactor, but without any gas flow. The oxygen sensor was introduced through septum.

## Discussion of the XPS data for the samples after OER

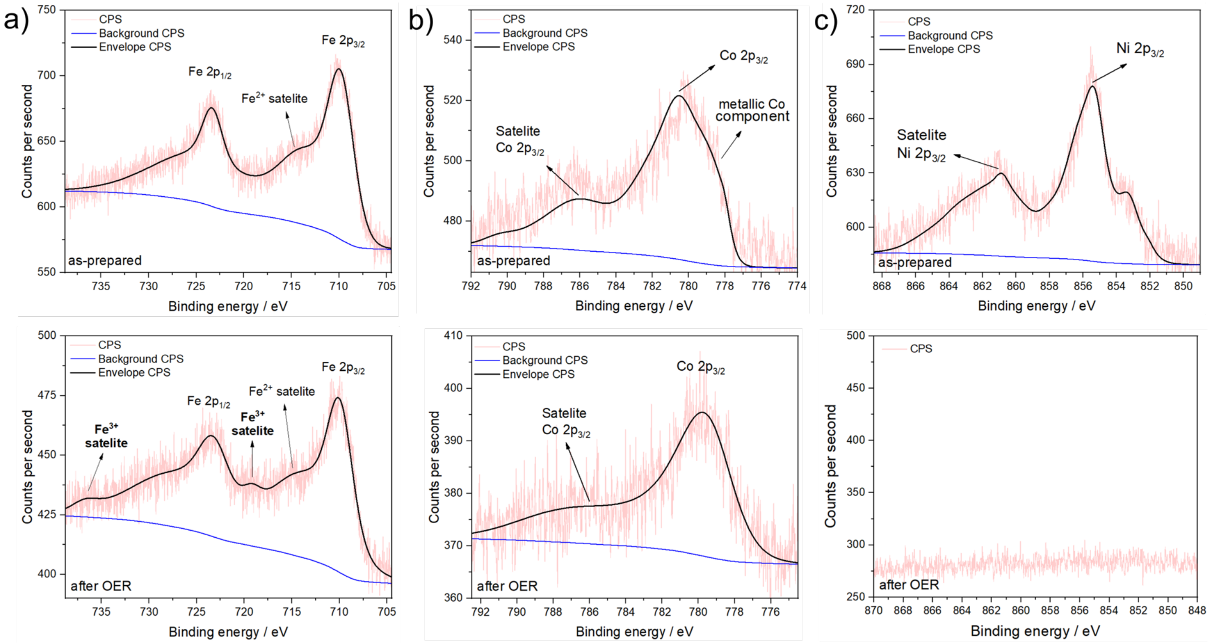

**Figure S13.** XPS spectra of the (a) $FeO_x$-$TiO_2$, (b) $CoO_x$-$TiO_2$ and (c) $NiO_x$-$TiO_2$ composites before (upper raw) and after OER (lower raw).

XPS spectrum of the $FeO_x$-$TiO_2$ after photocatalytic reaction (**Figure S13a**) clearly indicates the increase of the signals corresponding to $Fe^{3+}$ species as can be seen from the appearing of the characteristic satellites at 719 and 737 eV. The spectrum after OER shows that $Fe^{2+}$ is still present in the composite as one of the main components, but we can clearly suggest that some of the initial $Fe^{2+}$ species oxidized during the photocatalytic process (the samples prepared for these XPS measurements were exposed to 1h-long illumination under OER conditions).

XPS spectrum of the $CoO_x$-$TiO_2$ after reaction (**Figure S13b**) also indicates that oxidation of the initially present Co species takes place. As such, we do not anymore observe the shoulder at 778 eV (corresponding to small amount of metallic Co potentially present in the as-prepared composite), while the satellite at 786 eV gets effectively reduced implying that some of the $Co^{2+}$ species (e.g. the suggested $Co(OH)_2$) turn into $Co^{3+}$ during the photocatalytic OER.

XPS spectrum of the $NiO_x$-$TiO_2$ after OER (**Figure S13c**) marks strong differences to the other samples investigated after reaction: no signal characteristic for NiO/Ni species can be observed anymore. This cannot be related to composite instability or potential leaching of the Ni species into the solution under photocatalytic conditions as the XPS data after HER experiment clearly shows that Ni signal is preserved even after 14 hour light illumination run. We believe that this specialty of the $NiO_x$-$TiO_2$ is related to the role of $NiO_x$ species in OER and associated with the electron reduction of $Ag^+$ that was used as sacrificial agent. Given that XPS is a surface sensitive technique, we suggest that metallic Ag – being the product of $Ag^+$ reduction, as also confirmed by XPS – gets deposited onto $NiO_x$ sites that act as electron acceptor and release centres. This Ag shell effectively blocks the Ni sites not allowing for any XPS analyses.

This result highlights the differences between $NiO_x$ and the other two co-catalysts active for OER in terms of their role in charge extraction and separation, however, would require an extended investigation to elaborate on this in light of the rest of the data.

**Table S2.** XPS fitting parameters

| | **$MnO_x$-$TiO_2$** | **$CoO_x$-$TiO_2$** | | | **$FeO_x$-$TiO_2$** | **$NiO_x$-$TiO_2$** | | |
|---|---|---|---|---|---|---|---|---|
| | *MnO* | Co metal* | *$Co(OH)_2$* | *$Co_3O_4$* | *FeO* | Ni metal† | *NiO* | *$Ni(OH)_2$* |
| | *$Mn^{2+}$* | *$Co^0$* | *$Co^{2+}$* | *$Co^{2+}$,$Co^{3+}$* | *$Fe^{2+}$* | *$Ni^0$* | *$Ni^{2+}$* | *$Ni^{2+}$* |
| **Peak 1 / eV** | 640.1 | 778.1 | 780.5 | 779.0 | 708.8 | 852.2 | 853.3 | 855.3 |
| % | 22.74 | 10.87 | 24.53 | 8.81 | 24.23 | 3.32 | 4.80 | 4.58 |
| FWHM | 1.40 | 1.00 | 2.30 | 1.61 | 2.05 | 1.20 | 1.20 | 1.00 |
| **Peak 2 / eV** | 641.0 | 781.1 | 782.3 | 780.3 | 710.1 | 855.9 | 855.0 | 856.0 |
| Peak 2 - Peak 1 / eV | 0.97 | 3.00 | 1.80 | 1.30 | 1.30 | 3.65 | 1.71 | 0.77 |
| % | 26.4 | 1.47 | 17.2 | 6.34 | 30.08 | 0.26 | 14.92 | 28.05 |
| FWHM | 1.40 | 3.30 | 2.8 | 1.97 | 2.46 | 3.00 | 3.10 | 2.50 |
| **Peak 3 / eV** | 642.0 | 783.10 | 786.1 | 781.6 | 711.3 | 858.2 | 860.4 | 858.1 |
| Peak 3 - Peak 1 / eV | 1.90 | 5.00 | 5.59 | 2.60 | 2.50 | 6.03 | 7.15 | 2.79 |
| % | 20.96 | 1.08 | 21.46 | 3.31 | 14.57 | 0.50 | 11.52 | 1.88 |
| FWHM | 1.40 | 3.30 | 4.2 | 2.60 | 2.46 | 3.00 | 3.60 | 1.40 |
| **Peak 4 / eV** | 642.9 | - | 790.5 | 784.6 | 712.5 | - | 863.5 | 860.8 |
| Peak 4 - Peak 1 / eV | 2.85 | - | 9.99 | 5.6 | 3.70 | - | 10.25 | 5.58 |
| % | 11.85 | - | 1.56 | 1.77 | 25.52 | - | 1.21 | 0.88 |
| FWHM | 1.40 | - | 2 | 4.00 | 4.50 | - | 1.80 | 0.80 |
| **Peak 5 / eV** | 644.1 | - | - | 788.9 | 715.8 | - | 865.5 | 861.8 |
| Peak 5 - Peak 1 / eV | 3.99 | - | - | 9.9 | 7.00 | - | 12.25 | 6.58 |
| % | 4.47 | - | - | 1.58 | 5.61 | - | 1.31 | 24.45 |
| FWHM | 1.40 | - | - | 3.00 | 2.55 | - | 2.80 | 4.71 |
| **Peak 6 / eV** | 645.8 | - | - | - | - | - | - | 864.9 |
| Peak 6 - Peak 1 / eV | 5.74 | - | - | - | - | - | - | 9.59 |
| % | 13.6 | - | - | - | - | - | - | 2.31 |
| FWHM | 1.40 | - | - | - | - | - | - | 3.10 |
| % species | 100 | 13.42 | 64.75 | 21.81 | 100 | 4.08 | 33.76 | 62.15 |

*line shape LA(1.2,5,5)

†line shape LA(1.1,2.2,29)

**Table S3.** XPS quantification data of the best fits: Ni, NiO and $Ni(OH)_2$. Ni 2p composition in atomic % before HER, after HER (still wet from the reaction) and after HER dried overnight.

| | **at.%** | | |
|---|---|---|---|
| | *before* | *after(wet)* | *after(dry)* |
| **Ni** | 3.4 | 16.7 | 9.2 |
| **NiO** | 33.6 | 0.0 | 31.3 |
| **$Ni(OH)_2$** | 63.0 | 83.3 | 59.5 |

## References

1 C. Y. Xu, P. X. Zhang and L. Yan, *Journal of Raman Spectroscopy*, 2001, **32**, 862–865.

2 G. Liu, C. Sun, H. G. Yang, S. C. Smith, L. Wang, G. Q. (Max) Lu and H.-M. Cheng, *Chem. Commun.*, 2010, **46**, 755–757.

3 X. Cheng, X. Yu, Z. Xing and L. Yang, *Arabian Journal of Chemistry*, 2016, **9**, S1706–S1711.

4 J. C. Parker and R. W. Siegel, *Appl. Phys. Lett.*, 1990, **57**, 943–945.

5 S. Bernardini, F. Bellatreccia, A. C. Municchia, G. D. Ventura and A. Sodo, *Journal of Raman Spectroscopy*, 2019, **50**, 873–888.

6 J. Li, G. Lu, G. Wu, D. Mao, Y. Guo, Y. Wang and Y. Guo, *Catal. Sci. Technol.*, 2014, **4**, 1268–1275.

7 L.-N. Han, L.-B. Lv, Q.-C. Zhu, X. Wei, X.-H. Li and J.-S. Chen, *Journal of Materials Chemistry A*, 2016, **4**, 7841–7847.